Solid State Phenomena Vols. 108-109 (2005) pp. 577-584
online at http://www.scientific.net

Local measurements of diffusion length and chemical character of metal clusters in multicrystalline silicon

T. Buonassisi[1,a], A.A. Istratov[1,b], M.A. Marcus[2,c], M. Heuer[1,d], M.D. Pickett[1,e], B. Lai[3,f], Z. Cai[3,g], S.M. Heald[4,h], and E.R. Weber[1,i]

[1]Department of Materials Science and Engineering, University of California, Berkeley and Materials Science Division, Lawrence Berkeley National Laboratory, Berkeley, CA 94720, USA

[2]Advanced Light Source, Lawrence Berkeley National Laboratory, Berkeley, CA 94720, USA

[3]Advanced Photon Source, Argonne National Laboratory, Argonne, Illinois 60439, USA

[4]Pacific Northwest National Laboratory, Richland, WA 99352, USA

[a]buonassisi@alumni.nd.edu, [b]istratov@berkeley.edu, [c]mamarcus@lbl.gov, [d]heuer@berkeley.edu, [e]mpickett@berkeley.edu, [f]blai@aps.anl.gov, [g]cai@aps.anl.gov, [h]steve.heald@pnl.gov, [i]weber@berkeley.edu

Keywords: Copper, Gettering, Iron, Metal impurity precipitates, Nickel, Solar cells, Synchrotron, X-ray absorption spectroscopy, X-ray fluorescence.

Abstract. We present a comprehensive description of synchrotron-based analytical microprobe techniques used to locally measure the diffusion length and chemical character of metal clusters in multicrystalline silicon (mc-Si) solar cell material. The techniques discussed are (a) X-ray fluorescence microscopy, capable of determining the spatial distribution, elemental nature, size, morphology, and depth of metal-rich particles as small as 30 nm in diameter; (b) X-ray absorption microspectroscopy, capable of determining the chemical states of these metal-rich precipitates, (c) X-ray beam induced current (XBIC), which maps the minority carrier recombination activity, and (d) Spectrally-resolved XBIC, which maps the minority carrier diffusion length. Sensitivity limits, optimal synchrotron characteristics, and experimental flowcharts are discussed. These techniques have elucidated the nature and effects of metal-rich particles in mc-Si and the physical mechanisms limiting metal gettering from mc-Si, and have opened several promising new research directions.

Introduction

One decade ago, McHugo and Thompson [1-4] first recognized the potential applications of synchrotron-based analytical microprobe techniques to study the nature, distribution, and behavior of metal-rich particles in multicrystalline silicon (mc-Si). These techniques were further developed through the contributions of several individuals associated with the research group of Prof. E. R. Weber at the University of California, Berkeley [5-10]. More recently, the potential of these techniques has begun to be explored by other research groups around the world [11]. In this article, the principle distinguishing features of synchrotron-based analytical techniques are described, followed by a brief summary of research on metals in mc-Si conducted using these techniques.

Synchrotron-Based X-ray Microprobe Techniques

X-ray Fluorescence Microscopy (μ-XRF). Synchrotron-based X-ray fluorescence microscopy (μ-XRF), also known as "Scanning μ-XRF" (μ-SXRF), is used to detect and characterize the elemental compositions, sizes, and depths of metal-rich clusters. μ-XRF is similar to energy dispersive X-ray microanalysis (EDX) in that a focused beam excites core electrons from atoms within the sample, provoking the decay of electrons from higher-energy orbitals and the emitting of a characteristic series of X-rays, which are captured and quantified by an X-ray detector.

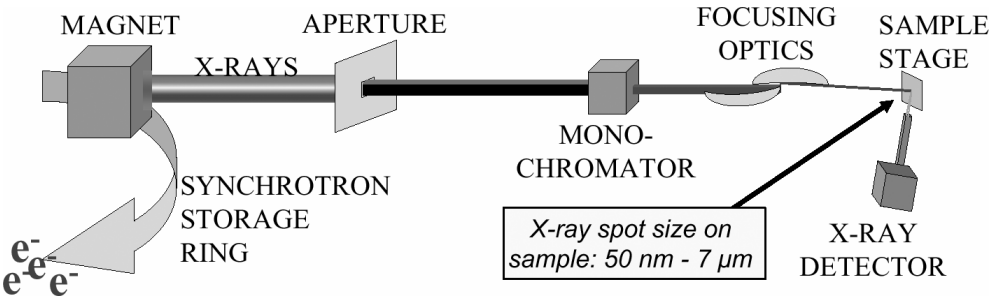

Figure 1: Schematic of an X-ray fluorescence microscopy (μ-XRF) beamline.

Nonetheless, μ-XRF is fundamentally different from EDX and is much more sensitive to impurities:

(a) *Higher sensitivity*: In μ-XRF, the excitation beam is an intense, synchrotron-generated, microfocused X-ray beam of 10^9–10^{12} photons/s. The photon-in, photon-out nature of μ-XRF produces negligible Bremsstrahlung background, resulting in orders of magnitude higher sensitivity than EDX. μ-XRF systems can detect as few as 10^{14} impurity atoms/cm^2 in one second (Fig. 2).

(b) *2-D mapping*: 2-dimensional impurity mapping is an integral part of synchrotron-based μ-XRF. As a a sample stage moves the sample in the X-Y directions, a spectrum is accumulated at each point by an X-ray detector (Fig. 1). The intensity of a given fluorescence peak can be plotted in two dimensions (Table I). In theory, EDX can also do 2-D mapping, but the lower bulk sensitivities of EDX compared to XRF generally require a longer data accumulation time per point, drastically increasing scan times. 2-D impurity mapping makes μ-XRF an ideal technique for detecting impurity-rich particles in low spatial concentrations, typical of mc-Si samples. Additionally, the elastically scattered peak intensity can be used to map grain structure in multicrystalline samples.

(c) *Spatial resolution*: The lateral resolution of μ-XRF is limited by the diameter of the incoming X-ray beam, which can be as small as ~50 nm. EDX is also limited by the beam diameter for very thin samples, thus EDX performed in a transmission electron microscope (TEM) can characterize single rows of atoms. However, for thicker (bulk) samples characterized by EDX in a scanning electron microscope (SEM), electron scattering within the sample creates a "generation volume" that can be as wide as 1 μm, effectively limiting the spatial resolution. The excellent spatial resolution makes μ-XRF ideal for determining the spatial and size distributions of sub-micron

Table I: Summary of Synchrotron-Based Analytical Microprobe Techniques

Acronym	**μ-XRF**	**μ-XAS**		**XBIC**	
Technique Name(s)	X-ray fluorescence microscopy	X-ray absorption microspectroscopy		X-ray beam induced current	
Sub-tech-nique(s)	μ-SXRF: Scanning μ-XRF. Often used interchangeably with μ-XRF.	XANES: X-ray absorption near-edge spectroscopy.	EXAFS: Extended x-ray absorption fine structure.	(Traditional) XBIC	SR-XBIC: Spectrally resolved XBIC
Deliv-erables	Elemental composition, size, morphology, depth, and spatial distribution of metal-rich particles. Grain boundary structure from elastically scattered peak.	Dependent on local unoccupied density of states (function of local bonding).	Structural info: Distances and # of electrons of nearest neighbor atoms.	Recombination activity map, analogous to simple LBIC.	Minority carrier diffusion length map, analogous to spectrally resolved LBIC.
Example	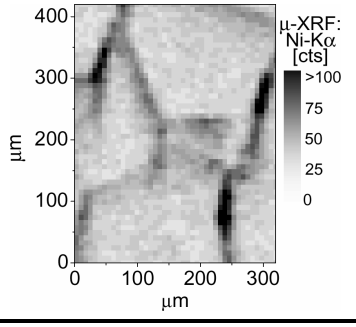	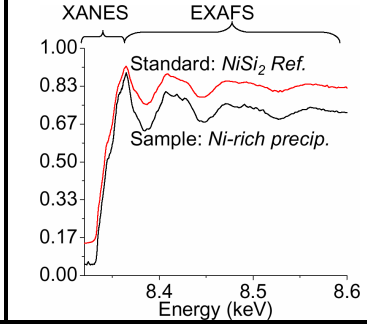		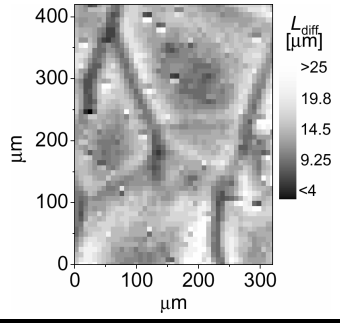	

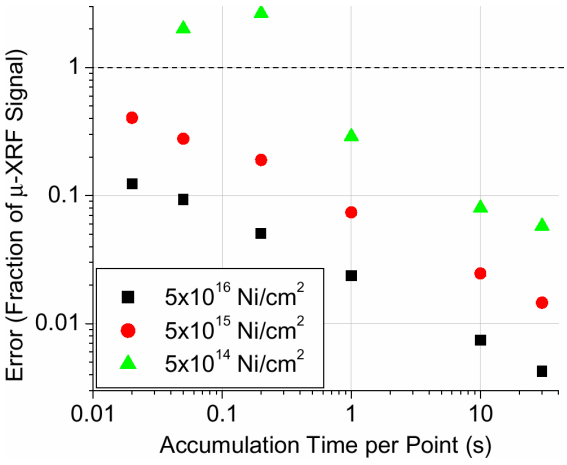

Figure 2: The bulk sensitivity (defined as the error of the signal w.r.t. background) of μ-XRF can be as high as 10^{14} Ni atoms per cm^2 for one second accumulation time per point (typical for large maps). For a circular X-ray spot size 200 nm in diameter, this equates into 1.26×10^5 Ni atoms.

impurity particles in thick samples.

(d) *Greater information depth*: In EDX, the information depth is limited by the penetration of electrons into the silicon sample (~10 μm for 40 keV electrons). In μ-XRF, the incoming X-ray beam has a higher energy than the resulting fluorescence, hence the information depth is chiefly limited by the attenuation length (distance through a material after which the beam intensity is reduced to 1/e of the original intensity; the information depth) of the *outgoing* fluorescence. Attenuation lengths of fluorescence energies of several common impurity elements in mc-Si are shown in Fig. 3. Spectroscopy of light elements such as oxygen and carbon are limited to the first monolayers of material, while detection of transition metal species extends as deep as hundreds of microns. The large information depth of μ-XRF makes it an ideal tool to study metal-rich particles in mc-Si.

(e) *Depth determination*: μ-XRF can determine the depth of an impurity particle within a Si matrix using two methods. The first method, known as the "rotation technique" [12], takes advantage of the 45° angle of entry of the X-ray beam relative the sample surface normal, comparing the relative shift of a particle in the bulk versus a surface feature for the sample mounted at 0° and 180°. This technique requires no information about the chemical state of the particle, but requires two μ-XRF maps, is limited by the spatial resolution of the beam, and requires a surface reference feature. The second technique to determine the depth of an impurity particle requires only a μ-XRF point scan, but also requires an additional reference sample with the same chemical composition as the impurity precipitate. Since the attenuation length of X-rays in silicon (α) varies as a function of X-ray fluorescence energy (E), the measured XRF count rates ($C_{Measured}$) for the Kα and Kβ fluorescence peaks of a particle in the bulk will be different than at the sample surface ($C_{Surface}$). The intensity of each peak for a particle beneath the surface will vary as a function of depth (d), as

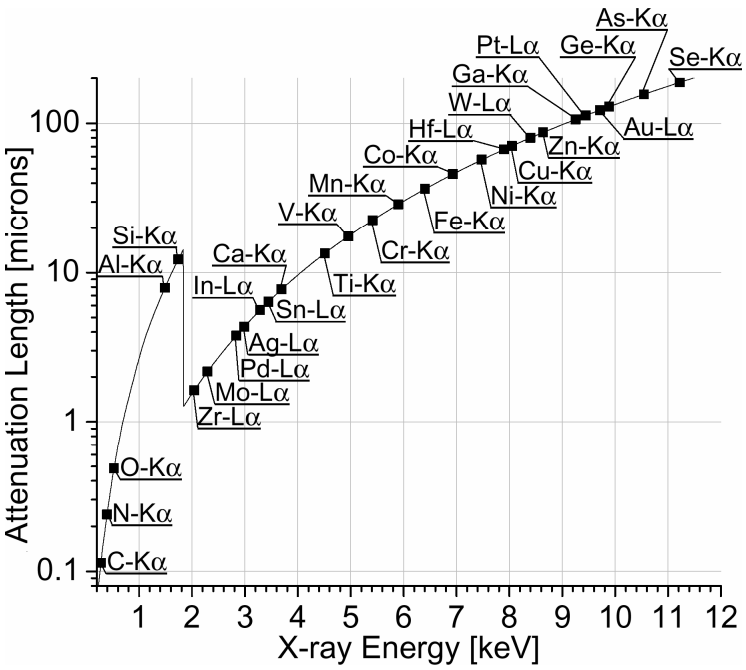

Figure 3: X-ray attenuation length in silicon as a function of X-ray energy. Square markers and labels indicate the fluorescence energies of impurity elements of interest in mc-Si. Larger attenuation lengths mean that the fluorescence signal can travel farther within the silicon matrix, increasing the information depth.

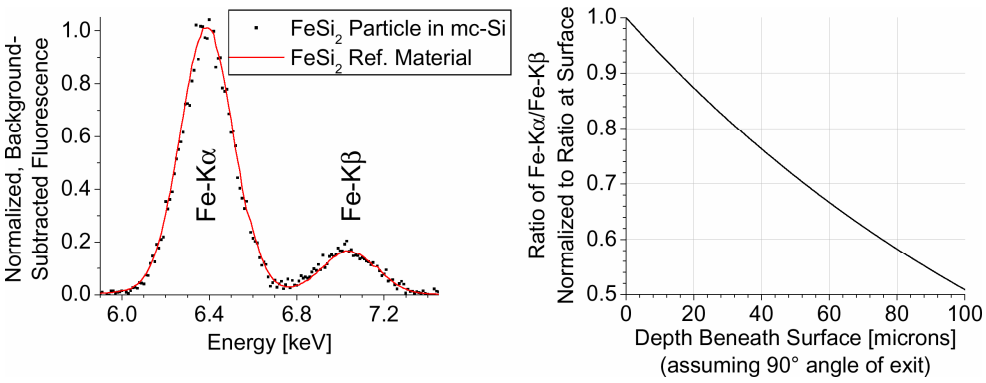

Figure 4: Left: An $FeSi_2$ precipitate is determined to be very near the sample surface by comparing Fe-Kα and Fe-Kβ peak heights. Right: The theoretical ratio of peak heights as a function of depth for iron, per Eq. 2.

$$C_{\mathrm{K}\alpha\ \mathrm{Measured}}\,(\mathrm{cts/s}) = C_{\mathrm{K}\alpha\ \mathrm{Surface}}\,(\mathrm{cts/s}) \cdot \exp\left(\frac{-d\ (\mathrm{cm})}{\alpha_{(E=\mathrm{K}\alpha)}\ (\mathrm{cm})}\right), \qquad \text{[Eq. 1]}$$

and likewise for Kβ. Solving for d, using Eq. 1 for Kα and Kβ peaks, we obtain

$$d = \left(\frac{\alpha_{(E=\mathrm{K}\alpha)} \cdot \alpha_{(E=\mathrm{K}\beta)}}{\alpha_{(E=\mathrm{K}\alpha)} - \alpha_{(E=\mathrm{K}\beta)}}\right) \cdot \ln\left(\frac{C_{\mathrm{K}\alpha\ \mathrm{Measured}} \cdot C_{\mathrm{K}\beta\ \mathrm{Surface}}}{C_{\mathrm{K}\beta\ \mathrm{Measured}} \cdot C_{\mathrm{K}\alpha\ \mathrm{Surface}}}\right), \qquad \text{[Eq. 2]}$$

where the ratio $(C_{\mathrm{K}\beta\ \mathrm{Surface}})\ /\ (C_{\mathrm{K}\alpha\ \mathrm{Surface}})$ is determined from μ-XRF measurement on the standard reference sample of identical chemical state, while ensuring identical detector positioning.

Since the ratio of Kα and Kβ X-ray fluorescence peak intensities for a particle beneath the surface will vary in a predictable manner compared to a standard reference sample, this technique provides a very accurate measure of the depth of an impurity particle (Fig. 4).

(f) *Standard-calibrated, quantified measurement of impurity particles in the bulk*: Particles with sizes larger than the beam spot size can be mapped in high resolution to determine their dimensions. In addition, the dimensions of a particle smaller than the beam spot size can also be determined: Knowing the depth of an impurity particle (and thus, the attenuation of the exiting X-ray fluorescence), and calibrating the μ-XRF count rate with a standard material with known impurity concentration (typically a NIST SRM 1832 or 1833 foil), it is possible to determine the number of impurity atoms comprising the particle by using the equation:

$$N_{\mathrm{Prec}}\ (\mathrm{atoms}) = \frac{C_{\mathrm{Prec}}\ (\mathrm{cts/s})}{C_{\mathrm{Std}}\ (\mathrm{cts/s})} \cdot [\mathrm{M}]_{\mathrm{Std}}\ (\mathrm{g/cm^2}) \cdot D_{\mathrm{Std}}\ (\mathrm{atoms/g}) \cdot A\ (\mathrm{cm^2}) \quad , \qquad \text{[Eq. 3]}$$

from Ref. [8], where N_{prec} is the number of atoms in a precipitate, C_{prec} is the XRF count rate with the beam focused on the precipitate and adjusted for the depth of the particle, C_{std} is the XRF count rate of the standard sample, $[\mathrm{M}]_{\mathrm{Std}}$ is the known metal concentration within the standard, D_{Std} is the density of the standard material in terms of atoms/g, and A is the X-ray beam spot size.

Knowing the density of the particle, it is possible to determine its (spherical) size:

$$R_{\mathrm{Prec}}\ (\mathrm{cm}) = \left(\frac{3}{4\pi} \cdot \frac{N_{\mathrm{Prec}}\ (\mathrm{atoms})}{D_{\mathrm{Prec}}\ (\mathrm{atoms/cm^3})}\right)^{1/3} \quad , \qquad \text{[Eq. 4]}$$

from Ref. [8], where R_{Prec} is the radius of the precipitate, and D_{Prec} is the density of impurity atoms within that precipitate (a function of chemical state).

X-ray Absorption Microspectroscopy (μ-XAS). Once μ-XRF locates a metal-rich particle, the X-ray absorption microspectroscopy (μ-XAS) technique – also known as X-ray absorption fine structure microanalysis (μ-XAFS) – is employed to determine its chemical state. While the X-ray beam position is fixed on the particle of interest, the X-ray beam energy is changed in increments of 0.25 – 5 eV using a monochromator. X-ray absorption by the particle is measured at each energy, providing an absorption spectrum like that shown in Table I. For thin bulk samples, absorption can be measured directly, by monitoring the intensity of the transmitted X-ray beam with an ion chamber. For a tiny particle within a silicon matrix, the absorption can be determined indirectly by using an X-ray detector to measure the impurity fluorescence intensity (a function of absorption).

X-ray absorption spectra are divided into two energy regions (per Table I), and each provides unique physical information. As X-ray photons begin to excite bound electrons into the lowest dipole-allowed unoccupied electronic states, one observes the X-ray absorption near edge structure (XANES) – also called near-edge X-ray absorption fine structure (NEXAFS). The local electronic environment surrounding an impurity atom dominates this region of the X-ray absorption spectrum. Oxidation state, degree of covalent or ionic bonding, and coordination number are factors that heavily influence XANES and depend on local bonding. Hence XANES is a good "fingerprint" method for determining the chemical state of an impurity particle in mc-Si [8, 13]. The extended X-ray absorption fine structure (EXAFS, up to a few hundred eV above the absorption edge) contains additional structural information. At those higher X-ray energies, core electrons are excited in a sphere-like wavefunction, partially scattering off neighboring atoms and interfering with the outgoing wavefunction, forming a standing wave that determines the amount of X-ray absorption by the central impurity atom. Thus, the EXAFS spectrum contains information about nearest neighbor distances and atomic weights [14], enabling the characterization of unknown structures.

X-ray Beam Induced Current (XBIC). It is impractical to map an entire $(2\times10^8$ nm$)^2$ mc-Si wafer with a high-resolution, 200 nm step size. Thus, it is useful to have a technique at the μ-XRF beamline capable of quickly mapping large sample areas to identify regions of interest, which can then be scanned with high-resolution μ-XRF. Such a technique has been developed in-situ, at the μ-XRF beamline, and is known as X-ray beam induced current (XBIC, Ref. [5, 15]). Since an impurity particle can have a space-charge region affecting the electronic properties of a much larger sample volume than the particle size, mapping the minority carrier current collection efficiency is a very useful approach to determine the locations of recombination-active defects in large-area samples.

XBIC functions very much like the electron or light beam induced current techniques (EBIC or LBIC, respectively), except that an intense synchrotron-generated X-ray beam is used to excite minority carriers instead of an electron beam or visible light. The collection efficiency of photo-excited carriers is measured using a pn-junction or Schottky diode on the surface of the mc-Si sample. Since XBIC is similar in physical principle to LBIC or EBIC, these techniques reveal the same recombination-active defects. For example, a region of interest identified in an LBIC map can be scanned using μ-XRF, with XBIC serving as the bridge between these two techniques [16].

Spectrally-Resolved X-ray Beam Induced Current (SR-XBIC). The XBIC technique is very useful for locating the positions of recombination-active defects, and even quantifying their recombination activity via the contrast between “good” and “bad” regions of material [6]. However, without calibrating the XBIC signal (which would require determining the exact internal quantum XBIC collection efficiency at a given energy), it is not possible to extract a quantified minority carrier diffusion length. Thus, with XBIC alone, it is very difficult to determine absolute changes within a sample or between two or more samples.

The spectrally-resolved XBIC (SR-XBIC) technique [17] produces a map of the minority carrier diffusion length, in much the same way as SR-LBIC. Several XBIC maps are acquired using different incoming X-ray energies. By relating the experimentally-measured photogenerated current collection efficiency to the X-ray penetration depth (function of energy), one precisely determines

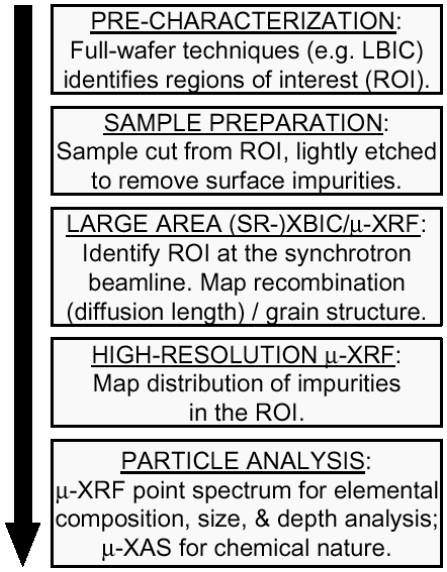

Fig. 5: Sample flowchart for synchrotron studies.

the minority carrier diffusion length. SR-XBIC injection conditions depend on the X-ray photon flux and energy, but are typically lower than or equal to typical LBIC systems [17].

The major advantage of SR-XBIC compared to other diffusion length measurement techniques is that it can be combined, in-situ, with μ-XRF and μ-XAS, thus establishing the correlation between metal particles and diffusion length with micron or sub-micron spatial resolution (Fig. 5, Table I). One can now quantitatively compare the local metal concentrations and diffusion lengths of different samples, or compare the same sample before and after a processing sequence.

Optimal Synchrotron Characteristics: There are over 30 synchrotrons worldwide, and the character (i.e. flux, energy bandwidth) of their X-rays depends on the acceleration voltage of the electrons in the storage ring, as well as the nature of the magnet in the storage ring used to deflect the electron beam and create the X-rays [18]. In synchrotrons with lower-energy storage rings (i.e. 1.5-3.5 GeV), a *bending magnet* is best-suited for producing X-rays with energies capable of fluorescing the K-shells of 3d transition metals. X-rays generated by the magnet are collimated down a *beamline* and focused by a set of mirrors or lenses onto the sample surface at the beamline *endstation* (Fig. 1). For the comparatively low fluxes generated by bending magnets, *X-ray mirrors* are typically used for focusing since they minimize flux loss while achieving micron-sized focusing conditions [19, 20]. On higher-energy storage rings (6-8 GeV), an *undulator* magnet can be used to produce a well-collimated, low bandwidth, high-flux beam of X-rays in the range of 4-12 keV, which enables the use of either X-ray mirrors [21] or high-definition *zone plate focusing optics* capable of achieving spot sizes smaller than 50 nm [22]. A tradeoff exists between small and large spot sizes: while the former is capable of detecting small particles, the latter is better-suited for scanning large sample areas. Thus, one frequently uses several synchrotron beamlines to study one sample [8, 13].

Synchrotron-based studies of metals in mc-Si

Nature and Impact of Metal Clusters in Mc-Si. Through numerous μ-XRF/XAS studies, at least two types of metal-rich particle in mc-Si solar cell material have been identified. The first type of particle frequently contains multiple metal species (often slow diffusers such as Ti and Ca), is frequently oxidized, and may be as large as several microns in diameter [2, 8, 23]. Based on their elemental compositions, chemical states, and large sizes, it is suspected that these are inclusions of foreign particles floating in the melt that are incorporated during crystal growth, and not precipitates forming from dissolved metals within the bulk [8, 13]. Because of their low spatial density, these particles are deemed to have a low direct impact on minority carrier diffusion length, although they can have a large indirect impact on solar cell performance via impurities dissolving and contributing to the formation of smaller precipitates and point defects [8]. The origins of these second-phase inclusion particles are indicated by their compositions, which can vary widely but generally indicate some combination of furnace parts (e.g. stainless steels, titanium, etc.), growth surfaces, and silicon feedstock material. The second type of metal-rich particle is the metal silicide nanoprecipitate, which is more numerically abundant than inclusions, and thus deemed to have a bigger direct impact on minority carrier diffusion length. Metal silicide nanoprecipitates are believed to form from dissolved metals, as they are frequently found at structural defects, which provide lower energy barriers for precipitate nucleation. Key to improving device performance is the proper

control over these smaller, more distributed metal-related defects, which include metal point defects, metal atoms segregated to structural defects, and metal silicide nanoprecipitates [8].

Processing-Induced Metal Defect Interactions. Since the majority of metal-rich particles in mc-Si are in a metal silicide chemical state, they should in principle be easy to getter, since their binding energy is small compared to oxidized compounds [1]. However, four important features make metals more difficult to getter from mc-Si materials than from single-crystalline silicon (sc-Si): (1) The total metal content in mc-Si contained in nanoprecipitates can be as high as $10^{14} – 10^{16}$ metal atoms cm^{-3} [8], thus many hours are needed at typical gettering temperatures to effectively dissolve and getter all metal silicide nanoprecipitates due to solubility and kinetic limintations [24]. Furthermore, (2) the gettering layers themselves have limited capacities and segregation coefficients for metals [13, 25, 26] and are typically very thin compared to the solar cell device thickness. The limited thickness and segregation coefficient of the gettering layer can result in between 0.1% – 10% of the original metal content remaining within the bulk after processing [13]. Additionally, (3) the interaction between metals and structural defects increases the solubility of metals within mc-Si relative to sc-Si [27-29], which in turn reduces the effective segregation coefficient of the gettering layer and results with more metals remaining inside the bulk. Finally, (4) several recent studies suggest that impurity defect interactions in mc-Si may affect solar cell efficiencies [6, 9, 30].These four processes combine to make the mechanics of gettering in mc-Si very different than for sc-Si. Neutron activation analysis studies have shown that between 10 – 40% of interstitial metals remain in the bulk after phosphorus diffusion gettering, as do nearly 100% of substitutional metals [31]. Material with high densities of structural defects are more severely affected by metal contamination [32], and typically do not improve as much during gettering [33] or hydrogen passivation [34].

Summary and Conclusions

A suite of synchrotron-based analytical microprobe techniques has been developed for impurity-rich particle detection and characterization in multicrystalline silicon. μ-XRF maps regions of mc-Si samples to determine the elemental nature and size, spatial, and depth distributions of metal-rich particles, and grain boundary structure. μ-XAS determines the chemical states of these metal-rich particles by comparison with standard reference material, in addition to identifying the structure of unknown compounds. XBIC and SR-XBIC map over large areas the recombination activity and minority carrier diffusion length, respectively. This not only allows one to determine the impact of a particular metal-rich particle on the electrical properties of the material, but also to incorporate materials characterization techniques based outside the synchrotron (e.g. LBIC), thus identifying regions of interest and maximizing productivity at the synchrotron.

Applications of these techniques to the study of metals in mc-Si have revealed two types of metal-rich particle: metal silicide nanoprecipitates and inclusions up to several microns in size, often consisting of several metals and/or in oxidized chemical state. These techniques have contributed to the understanding that gettering in mc-Si is limited by several physical phenomena, including metal – structural defect interactions as well as the limited capacity and segregation coefficient of the gettering layer. Impurity interactions, especially in the context of device processing, may cause unexpected evolutions in defect distributions and/or chemical states and promise fertile opportunities for future studies.

Acknowledgments: Discussions with and assistance of A.C. Thompson, O.F. Vyvenko, and S. Fakra are gratefully acknowledged. This work was supported by NREL Subcontract No. AAT-2-31605-03. The operations of the Advanced Light Source at Lawrence Berkeley National Laboratory and of the Advanced Photon Source at Argonne National Laboratory are supported by the Director, Office of Science, Office of Basic Energy Sciences, of the US Department of Energy under Contract

Numbers DEAC03-76SF00098 and W-31-109-ENG-38, respectively. One of the authors (M.H.) thanks the Deutsche Forschungsgemeinschaft for funding the project HE 3570/2-1.

References

[1] S.A. McHugo, A.C. Thompson, et al.: J. Appl. Phys. Vol. 89 (2001), p. 4282.
[2] S.A. McHugo, A. C. Thompson, I. Périchaud, and S. Martinuzzi: Appl. Phys. Lett. Vol. 72 (1998), p. 3482.
[3] S.A. McHugo: Appl. Phys. Lett. Vol. 71 (1997), p. 1984.
[4] S.A. McHugo, A.C. Thompson, et al.: Journal of Crystal Growth Vol. 210 (2000), p. 395.
[5] H. Hieslmair, A.A. Istratov, et al.: Proc. 10th NREL Workshop on Crystalline Silicon Solar Cell Materials and Processes (Copper Mountain, CO, USA, 2000), p. 162.
[6] O.F. Vyvenko, T. Buonassisi, A. A. Istratov, E. R. Weber, M. Kittler, and W. Seifert: J. Phys.: Condens. Matter Vol. 14 (2002), p. 13079.
[7] A.A. Istratov, H. Hieslmair, et al.: Solar Energy Materials & Solar Cells Vol. 72 (2002), p. 441.
[8] T. Buonassisi, A.A. Istratov, et al.: J. Appl. Phys. Vol. 97 (2005), p. 074901.
[9] M. Heuer, T. Buonassisi, et al.: submitted to Phys. Rev. Lett.
[10] C. Flink, S.A. Mchugo, et al.: Proc. 10th Workshop on Crystalline Silicon Solar Cell Materials and Processes, 2000), p. 212.
[11] Y. Ohshita, K. Arafune, et al.: Proc. 31st IEEE Photovoltaic Specialists Conference (Lake Buena Vista, FL, USA, 2005), p. 1269.
[12] O.F. Vyvenko, T. Buonassisi, et al.: J. Phys.: Condens. Matter Vol. 16 (2004), p. S141.
[13] T. Buonassisi, M.A. Marcus, et al.: J. Appl. Phys. Vol. 97 (2005), p. 063503.
[14] *X-ray Absorption: Principles, Applications, Techniques of EXAFS, SEXAFS and XANES*, ed. D.C. Koningsberger, and R. Prins. (Wiley-Interscience, Eindhoven, The Netherlands, 1988)
[15] O.F. Vyvenko, T. Buonassisi, et al.: J. Appl. Phys. Vol. 91 (2002), p. 3614.
[16] T. Buonassisi, O.F. Vyvenko, et al.: J. Appl. Phys. Vol. 95 (2004), p. 1556.
[17] T. Buonassisi, A.A. Istratov, et al.: Submitted to Appl. Phys. Lett. (2005.
[18] D. Attwood: *Soft X-rays and extreme ultraviolet radiation: Principles and applications*. (Cambridge University Press, Cambridge, UK, 2000)
[19] J.H. Underwood, A.C. Thompson, et al.: Nucl. Instr. and Meth. A Vol. 266 (1988), p. 318.
[20] M.A. Marcus, A.A. MacDowell, et al.: J. Synchrotron Radiation Vol. 11 (2004), p. 239.
[21] S.M. Heald, E.A. Stern, et al.: J. Synchrotron Rad. Vol. 8 (2001), p. 342.
[22] W. Yun, B. Lai, et al.: Rev. Sci. Instrum. Vol. 70 (1999), p. 2238.
[23] S.A. McHugo, A.C. Thompson, et al.: Physica B Vol. 273-274 (1999), p. 371.
[24] P.S. Plekhanov, R. Gafiteanu, U. M. Gosele, and T. Y. Tan: J. Appl. Phys. Vol. 86 (1999), p. 2453.
[25] H. Hieslmair, S.A. McHugo, et al.: in *Properties of Crystalline Silicon*, (Short Run Press, Exeter, 1999), p. 775.
[26] S.M. Myers, M. Seibt, and W. Schröter: J. Appl. Phys. Vol. 88 (2000), p. 3795.
[27] A.A. Istratov, W. Huber, and E.R. Weber: Appl. Phys. Lett. Vol. 85 (2004), p. 4472.
[28] R.C. Dorward and J.S. Kirkaldy: J. Mater. Sci. Vol. 3 (1968), p. 502.
[29] S.A. McHugo, E.R. Weber, et al.: Appl. Phys. Lett. Vol. 69 (1996), p. 3060.
[30] T. Buonassisi, M. Heuer, et al.: Proc. 20th European Photovoltaic Solar Energy Conference (Barcelona, Spain, 2005), p. in press.
[31] D. Macdonald, A. Cuevas, et al.: Proc. 29th IEEE Photovoltaic Specialists Conference (New Orleans, USA, 2002), p. 1707.
[32] S. Pizzini, L. Bigoni, et al.: J. Electrochem. Soc. (USA) Vol. 133 (1986), p. 2363.
[33] S.A. McHugo, H. Hieslmair, and E.R. Weber: Applied Physics A: Material Science & Processing Vol. 64 (1997), p. 127.
[34] S. Binetti, S. Ratti, et al.: Proc. 14th European Photovoltaic Solar Energy Conference (Barcelona, Spain, 1994), p. 709.